

A LARGE-SCALE SURVEY OF NGC 1333

ANDREW J. WALSH AND PHILIP C. MYERS

Harvard-Smithsonian Center for Astrophysics, Cambridge, MA; awalsh@cfa.harvard.edu

JAMES DI FRANCESCO

Herzberg Institute of Astrophysics, National Research Council of Canada, Victoria, BC, Canada

AND

SUBHANJOY MOHANTY, TYLER L. BOURKE, ROBERT GUTERMUTH, AND DAVID WILNER

Harvard-Smithsonian Center for Astrophysics, Cambridge, MA

Received 2006 August 24; accepted 2006 October 11

ABSTRACT

We observed the clustered star forming complex NGC 1333 with the BIMA and FCRAO telescopes in the transitions $\text{HCO}^+(1-0)$ and $\text{N}_2\text{H}^+(1-0)$ over an $11' \times 11'$ area with resolution $\sim 10''$ (0.015 pc). The N_2H^+ emission follows very closely the submillimeter dust continuum emission, while HCO^+ emission appears more spatially extended and also traces outflows. We have identified 93 N_2H^+ cores using the CLUMPFIND algorithm, and we derive N_2H^+ core masses between 0.05 and $2.5 M_\odot$, with uncertainties of a factor of a few, dominated by the adopted N_2H^+ abundance. From a comparison with virial masses, we argue that most of these N_2H^+ cores are likely to be bound, even at the lowest masses, suggesting that the cores do not trace transient structures, and implies the entire mass distribution consists of objects that can potentially form stars. We find that the mass distribution of N_2H^+ cores resembles the field star IMF, which suggests that the IMF is locked in at the prestellar stage of evolution. We find that the N_2H^+ cores associated with stars identified from Spitzer infrared images have a flat mass distribution. This might be because lower mass cores lose a larger fraction of their mass when forming a star. Even in this clustered environment, we find no evidence for ballistic motions of the cores relative to their lower density surroundings traced by isotopic CO emission, although this conclusion must remain tentative until the surroundings are observed at the same high resolution as the N_2H^+ .

Subject headings: ISM: clouds — ISM: kinematics and dynamics — stars: formation

1. INTRODUCTION

Stars form predominantly within clusters inside turbulent molecular cores (Clarke et al. 2000), but there is no generally accepted theory of how this process occurs (Elmegreen et al. 2000). This deficiency is due in part to the lack of observational characterization of processes involved in cluster formation, given the wide range of scales that must be sampled simultaneously to provide a meaningful picture (e.g., 0.01–1.0 pc). Much recent work has focused on observations of isolated star formation. This is easy to understand as a star forming in isolation is not affected by any neighbors. However, in a clustered region, we usually see stars at different stages of formation, all within close proximity to each other, implying that there may be an effect of the older stars on the evolution of the youngest cluster members. An excellent example of this is NGC 1333, where Class 0, I, II, and III protostars exist, almost certainly along with prestellar cores. Trying to understand such a complicated region is much more difficult, but is a worthwhile pursuit because most stars form in clustered environments where these confusing factors appear. Thus, in order to understand the typical mode of star formation, it is necessary to understand star formation in a cluster such as NGC 1333.

NGC 1333 is a reflection nebula in Perseus which is associated with a molecular cloud, at a distance of 300 pc (de Zeeuw et al. 1999). It is also associated with two young star clusters identified in the near-infrared (Aspin et al. 1994; Lada et al. 1996). Furthermore, it appears that a significant proportion of the stars seen in the near-infrared are pre-main-sequence (Aspin et al. 1994; Aspin 2003). Figure 1 shows the $850 \mu\text{m}$ dust continuum emission toward NGC 1333, mapped by Sandell & Knee (2001; hereafter

SK01). Plus symbols mark the positions of dust continuum peaks, established by SK01. The majority of the emission is found in the southern half of NGC 1333, which includes the IRAS 4 complex, the IRAS 2 complex and the SSV¹ 13 complex. Each complex has previously been identified as a site of multiple star formation. NGC 1333 contains many well known outflows. Probably the best known is the outflow powered by SSV 13, or possibly the radio continuum source VLA 3 (Rodriguez et al. 1997). It is associated with the Herbig-Haro objects HH 7–11 to the southeast and extends into the central cavity of NGC 1333 to the northwest. In addition to this, there are outflows from both the IRAS 4 and 2 complexes, as well as IRAS 7 and 8 to the north.

SK01 note that the dust cores in NGC 1333 appear to have a mass function which is consistent with the stellar IMF. This has also been found for other regions of star formation such as in Ophiuchus (Motte et al. 1998; Johnstone et al. 2000) and IRAS 19410+2336 (Beuther & Schilke 2004). Recent theories for star formation (e.g., Bonnell et al. 2001b; Bate & Bonnell 2005) indicate the stellar initial mass function is created at an advanced stage of evolution—during the accretion phase as matter is deposited onto the pre-main-sequence star. Thus, the findings of stellar-like mass functions in prestellar cores is unexpected. One possible explanation is that the dust cores are transient phenomena and therefore are unlikely to be the sites of future generations of star formation. In order to decide whether such cores are transient or self-gravitating, it is necessary to observe cores in molecular

¹ We adopt the SSV designation for this source following Herbig & Jones (1983).

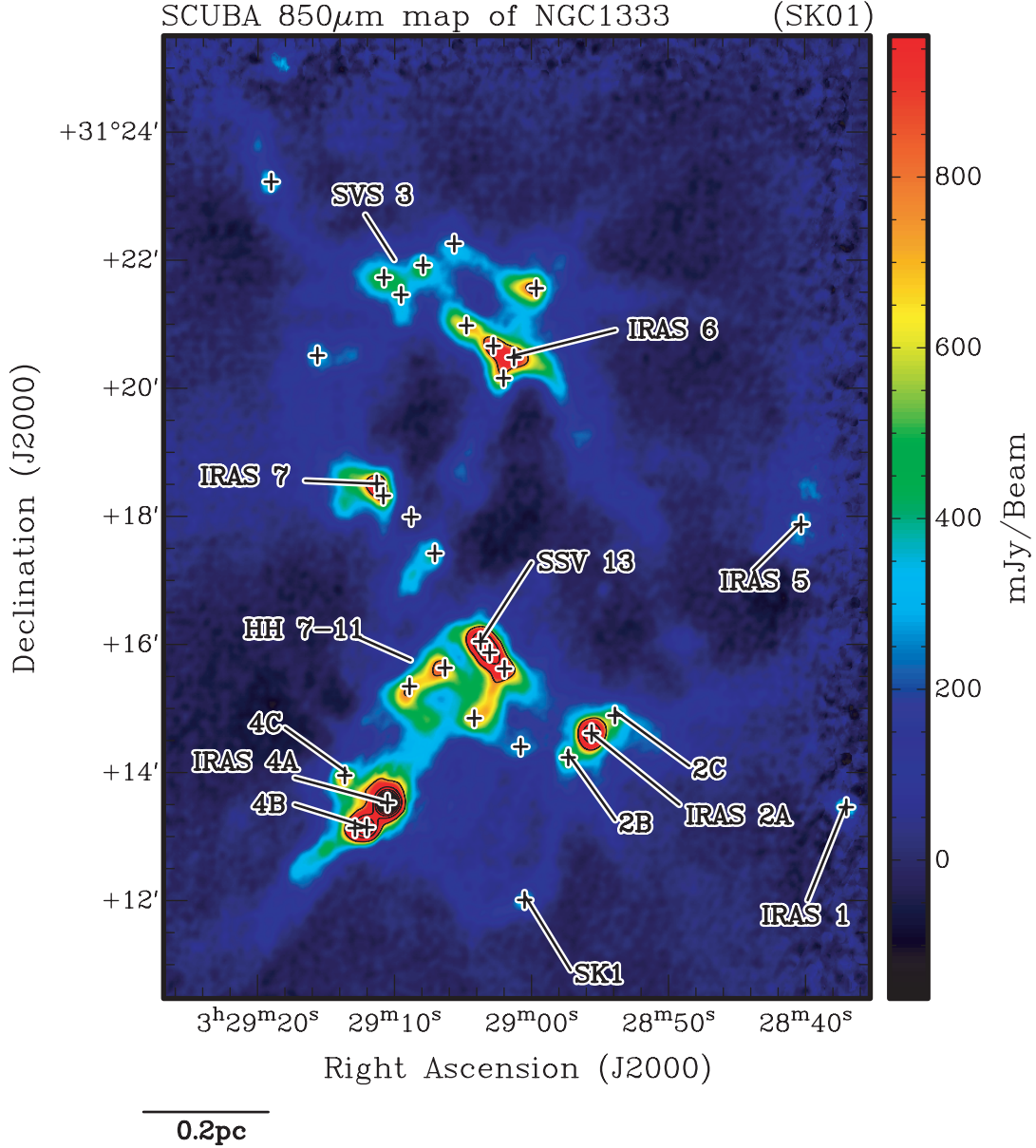


FIG. 1.— SCUBA 850 μ m dust continuum emission (SK01) in NGC 1333. Contours are 10%, 20%, 30%, ..., 90% of the peak 6.68 Jy beam $^{-1}$. Plus symbols indicate the positions of SCUBA continuum sources identified by SK01.

line tracers so that kinematic information may tell us about their internal motions.

2. OBSERVATIONS AND DATA REDUCTION

2.1. BIMA Observations

Observations of NGC 1333 were made with the 10-element Berkeley Illinois Maryland Association (BIMA) interferometer, at Hat Creek, CA, operating simultaneously at 89 and 93 GHz. The maps were made by mosaicking together 126 pointings spaced by $\sim 1'$. With a $\sim 2'$ FWHM primary beam at 3 mm, the resulting close-packed hexagonal pointing pattern provided full Nyquist sampling across the central $11' \times 11'$, yielding constant sensitivity across this field. The field was divided into two halves, with the southern half observed mostly in the fall of 2001, and the northern half observed in the spring of 2002. A total of 16 usable data tracks of 3–11 hr length were obtained over this period, in both the C and D configurations. Both $\text{HCO}^+(1-0)$ and $\text{N}_2\text{H}^+(1-0)$ were

observed in correlator windows of 256 channels each 0.16 km s $^{-1}$ wide. All seven hyperfine components of $\text{N}_2\text{H}^+(1-0)$ were observed in a single window. The remaining correlator windows were combined to provide 800 MHz bandwidth for simultaneous continuum observations.

We assume the line rest frequencies of 89.188253 GHz for $\text{HCO}^+(1-0)$ (Ulich & Haas 1976) and 93.176258 GHz for the “isolated” ($F_1F = 01-12$) $\text{N}_2\text{H}^+(1-0)$ hyperfine component (Lee et al. 2001).

2.2. FCRAO Observations

Observations of NGC 1333 were made with the Five College Radio Astronomy Observatory (FCRAO) 14 m telescope on 2002 November 16. The data were taken in an on-the-fly (OTF) mode² using SEQUOIA, which is a MMIC multibeam receiver with a

² See <http://donald.astro.umass.edu/~fcrao/library/manuals/otfmanual.html>.

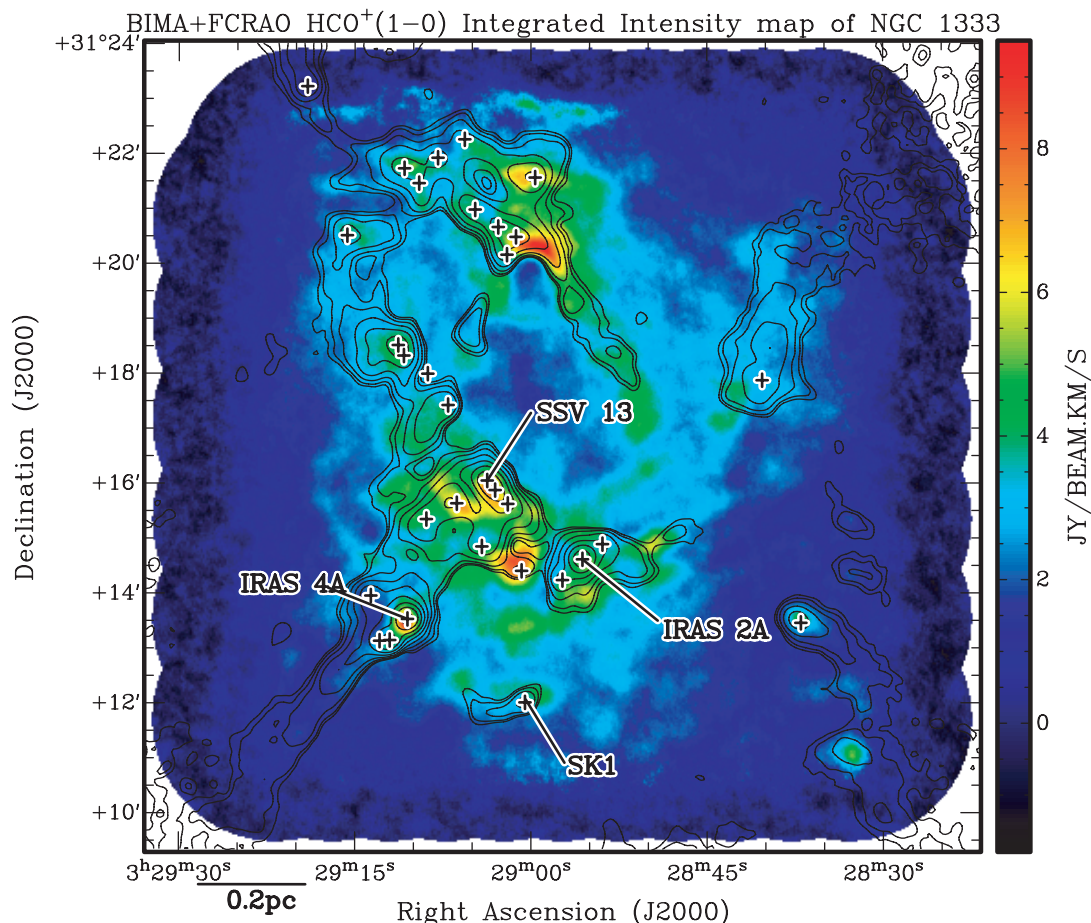


FIG. 2.— $\text{HCO}^+(1-0)$ integrated intensity map of NGC 1333: $0.2 \text{ Jy beam}^{-1} \text{ km s}^{-1} = 1 \sigma$. Contours are SCUBA $850 \mu\text{m}$ emission (SK01). Contour levels are 0.02, 0.04, 0.08, 0.16, ..., 5.12 Jy beam^{-1} , where $0.2 \text{ Jy beam}^{-1} = 1 \sigma$. Plus symbols indicate the positions of SCUBA continuum sources identified by SK01. HCO^+ emission is seen to cover a larger area than submillimeter continuum and loosely follows the submillimeter contours.

32 pixel array, arranged as two 4×4 arrays with orthogonal polarizations. Simultaneous observations were performed in $\text{N}_2\text{H}^+(1-0)$ and $\text{HCO}^+(1-0)$. The entire $11' \times 11'$ BIMA field was mapped with full Nyquist sampling. The FCRAO beam FWHM is about $50''$ for these observations. Typical rms noise values are 0.048 K for HCO^+ and 0.053 K for N_2H^+ . Average system temperatures for HCO^+ were 164 K and for N_2H^+ were 174 K. The spectrometer is a digital autocorrelator with 1024 channels. Our spectral resolution was 25 kHz, corresponding to about 0.08 km s^{-1} . We assumed a conversion factor of 43.7 Jy K^{-1} .

2.3. Combination of Interferometer and Single-Dish Data

The BIMA and FCRAO data were combined using the BIMA version of MIRIAD (Q. Zhang 2006, private communication). The FCRAO data were initially demosaicked into single pointings corresponding to the BIMA pointings. Each pointing was then deconvolved with the FCRAO beam. UV points were randomly generated across the UV plane, with UV distances from 0 to u_{max} , where u_{max} corresponds to the size of the FCRAO dish (radius 7 m). The density of points in the UV plane was chosen such that they match the density of UV points from the BIMA data. The demosaicked, deconvolved FCRAO data were then transformed into the UV plane. Only data corresponding to the randomly generated UV points were recorded. The FCRAO and BIMA UV data were then combined, imaged and cleaned using standard MIRIAD reduction techniques.

The 1σ rms sensitivities of the cleaned data are 3 mJy beam^{-1} for the continuum data, $330 \text{ mJy beam}^{-1}$ for both HCO^+ and N_2H^+ . The final synthesized beam FWHMs were $\sim 10''$ ($\sim 0.011 \text{ pc}$) for all data.

3. RESULTS

Figure 2 shows the $\text{HCO}^+(1-0)$ integrated intensity emission, compared to the $850 \mu\text{m}$ continuum emission. Some general correspondence is seen between the two. For example, many of the peaks seen in the continuum map correspond to HCO^+ peaks, including IRAS 4A, 4B, 2A, and SSV 13. Also, some large-scale structures show similar morphologies. On the other hand, some significant differences between the two are noticed: generally the HCO^+ emission appears to cover a larger area than the continuum emission. Although the continuum map has been filtered spatially due to chopping during observations, this is probably because the HCO^+ transition is more sensitive to lower column densities of material than the continuum observations. There are also differences in the distributions due to the effects of outflows which are discussed in § 3.1.

Figure 3 shows the $\text{N}_2\text{H}^+(1-0)$ integrated intensity emission, compared to the dust continuum emission. The distribution of N_2H^+ very closely follows that of the cold dust emission, much closer than that of the HCO^+ emission. This similarity shows that N_2H^+ is an excellent tracer of cold dust emission, as is known from studies of isolated cores (Tafalla et al. 2002). However, some

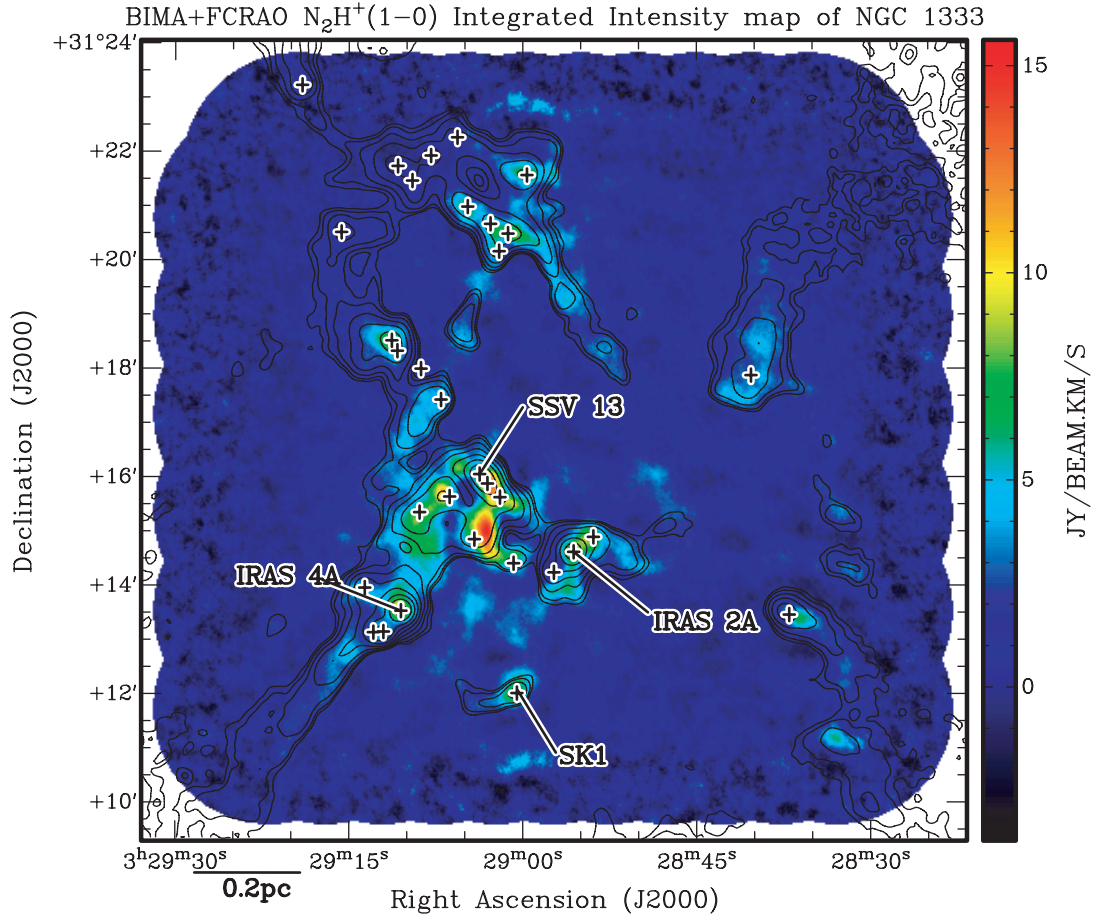


FIG. 3.—Same as Fig. 2, but for $N_2H^+(1-0)$. N_2H^+ and the submillimeter continuum closely follow each other in both extent and morphology. Small differences are seen between the two, however (e.g., IRAS 2A/B/C).

small differences can be seen in Figure 3: the brightest spot in the dust continuum map is IRAS 4A, which is over twice as bright as anything else in the field of view. However, the brightest spot in the N_2H^+ map is located an arcminute to the south of SSV 13. The IRAS 2 complex includes three dust continuum peaks 2B, 2A, and 2C running from southeast to northwest, respectively. While IRAS 2A is clearly the brightest in both continuum and N_2H^+ integrated intensity emission, IRAS 2C is a very weak continuum source but is almost as bright in N_2H^+ emission as IRAS 2A. Furthermore, IRAS 2B has stronger emission in continuum than IRAS 2C, but appears almost devoid of any N_2H^+ emission. Jørgensen et al. (2004a) have investigated the chemistry of N_2H^+ in this region and conclude that the apparent differences are due to varying degrees of thermal processing: 2B is the warmest and oldest source, having destroyed N_2H^+ around it, IRAS 2C is the youngest and coolest source with physical conditions that favor the production of N_2H^+ , and IRAS 2A has a temperature and age somewhere between the two. One other major difference between the continuum and N_2H^+ morphologies is that near SSV 3 (to the northeast of the field of view), there is a large region which clearly shows continuum emission consisting of at least five sources identified by SK01, spanning an area approximately $0.3' \times 0.2'$, but shows no evidence of N_2H^+ emission.

Figure 4 shows the first moment map of line of sight velocities for N_2H^+ . Most of the emission is found between velocities of 6.5 and 8.5 km s⁻¹. Overall, the emission in the southern part of NGC 1333 (south of 31° 14') appears blueshifted with respect to emission in other parts of the region. N_2H^+ emission close to

IRAS 7 appears to be redshifted from the bulk of the emission. Previously, Ho & Barrett (1980) suggested that bulk motions traced by ammonia were indicative of rotation. However, it appears their data were strongly biased by the redshifted emission associated with IRAS 7. If NGC 1333 were undergoing rotation, then we would expect to see redshifted emission over a much larger area, rather than being confined around IRAS 7. We still see a large area to the south with blueshifted emission, but apart from IRAS 7, the rest of the gas appears to be moving at approximately the same velocity. Therefore, the gas traced by N_2H^+ does not show significant signs of large-scale rotation, although there are clear differences between motions on smaller scales.

3.1. HCO⁺ Outflows

Knee & Sandell (2000) have previously described these outflows in detail, however we include Figure 5 which shows the blue and red lobes of outflows in the HCO⁺ map which shows the outflows at higher resolution than the maps of Knee & Sandell (2000). The blueshifted lobe from SSV 13 (or VLA 3) is clearly the brightest emission in the field of view.

Apart from the previously detected outflows, we note that the large, redshifted lobe of emission in the center of the field of view coincides with the central cavity (Knee & Sandell 2000). The central cavity is filled with high velocity gas from outflows and Knee & Sandell (2000) suggest it was created by these outflows. Furthermore, the red lobe coincident with the central cavity appears to be bounded by the filamentary structure of dense gas traced by N_2H^+ . We therefore conclude that the outflow(s) responsible

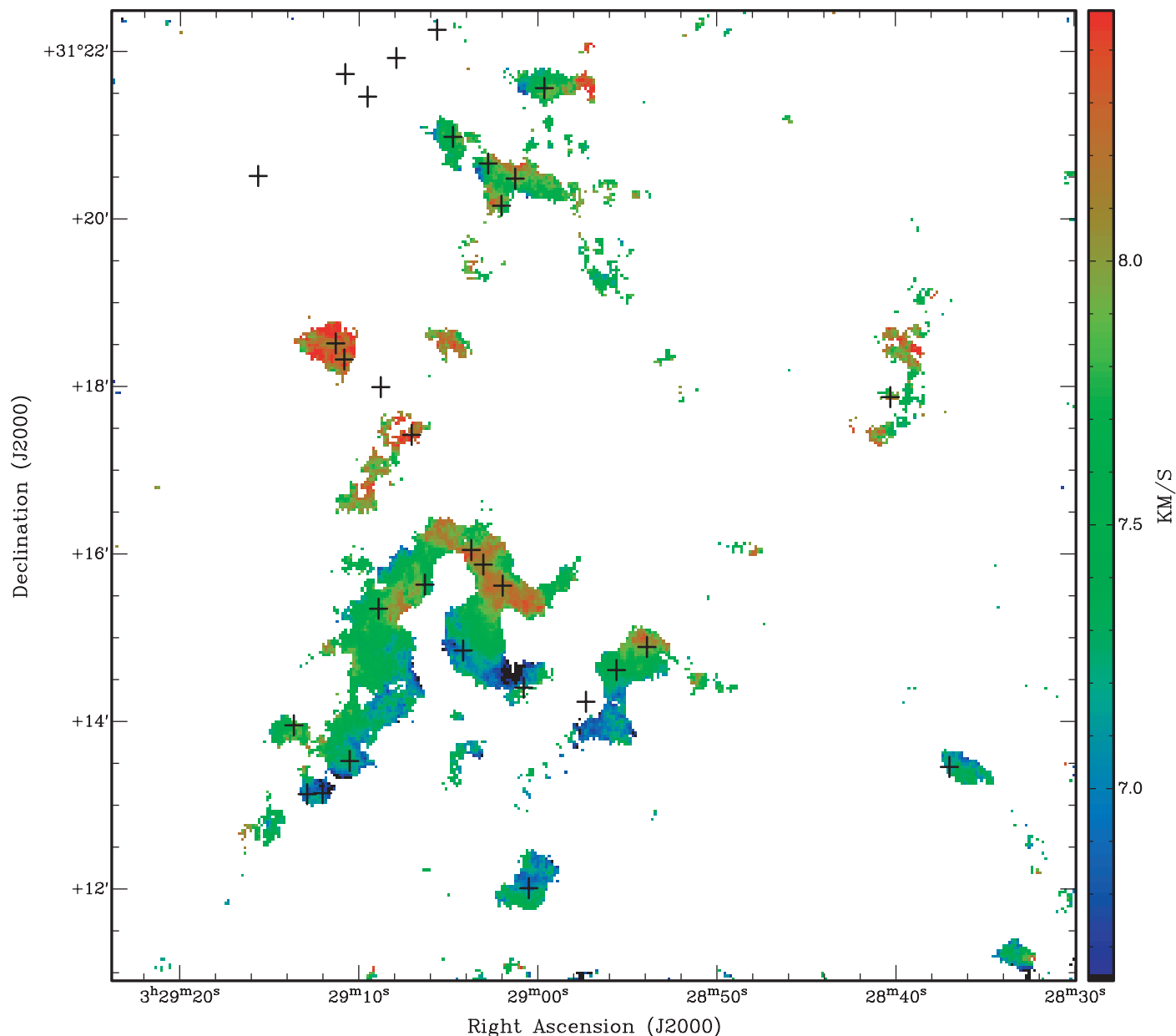


FIG. 4.— N_2H^+ first moment map of NGC 1333, showing the line-of-sight motions of the gas. Plus symbols indicate the positions of SCUBA continuum sources identified by SK01.

for this redshifted lobe fill the cavity with high velocity gas. It is clear that the bulk of this lobe comes from the outflow associated with either SSV 13 or VLA 3, but the north-south outflow from IRAS 2A also projects into this area, as well as the outflow from IRAS 7. It is even possible that there is a redshifted outflow lobe from SSV 13B, located to the west of SSV 13 that also projects into the cavity. These overlapping outflows make interpretation of the redshifted emission in this region difficult.

4. DISCUSSION

4.1. Analysis of N_2H^+ Cores

As previously mentioned, the N_2H^+ map very closely follows that of the dust continuum emission. Therefore we can analyze the density structure of NGC 1333 by observing the emission in this transition. Because N_2H^+ is a spectral line, we can also use the velocity information to help discriminate cores along the same line of sight. The $\text{N}_2\text{H}^+(1-0)$ transition has seven hyperfine compo-

nents that could potentially be used for better velocity determination of the cores; however, because most of these hyperfine components are blended, we choose to restrict our analysis to the isolated hyperfine component. This has the unfortunate effect of reducing our overall signal from this transition.

CLUMPFIND (Williams et al. 1994) is an algorithm for identifying peaks of emission in a data cube. It was originally used to identify clumps in single-dish spectra. It works in a way similar to contouring a map: where it finds closed contours a core is identified. The algorithm also extends the size of the core by including adjoining pixels down to a detection threshold. If a core is extended until it runs into another core (with its own separate peak), the algorithm stops extending the core on that front. The outcome is an interconnected cube of identified cores that appear similar to what would be expected if one identified cores and core boundaries by eye. Thus, all the real emission above the detection threshold is categorized as material belonging to some core.

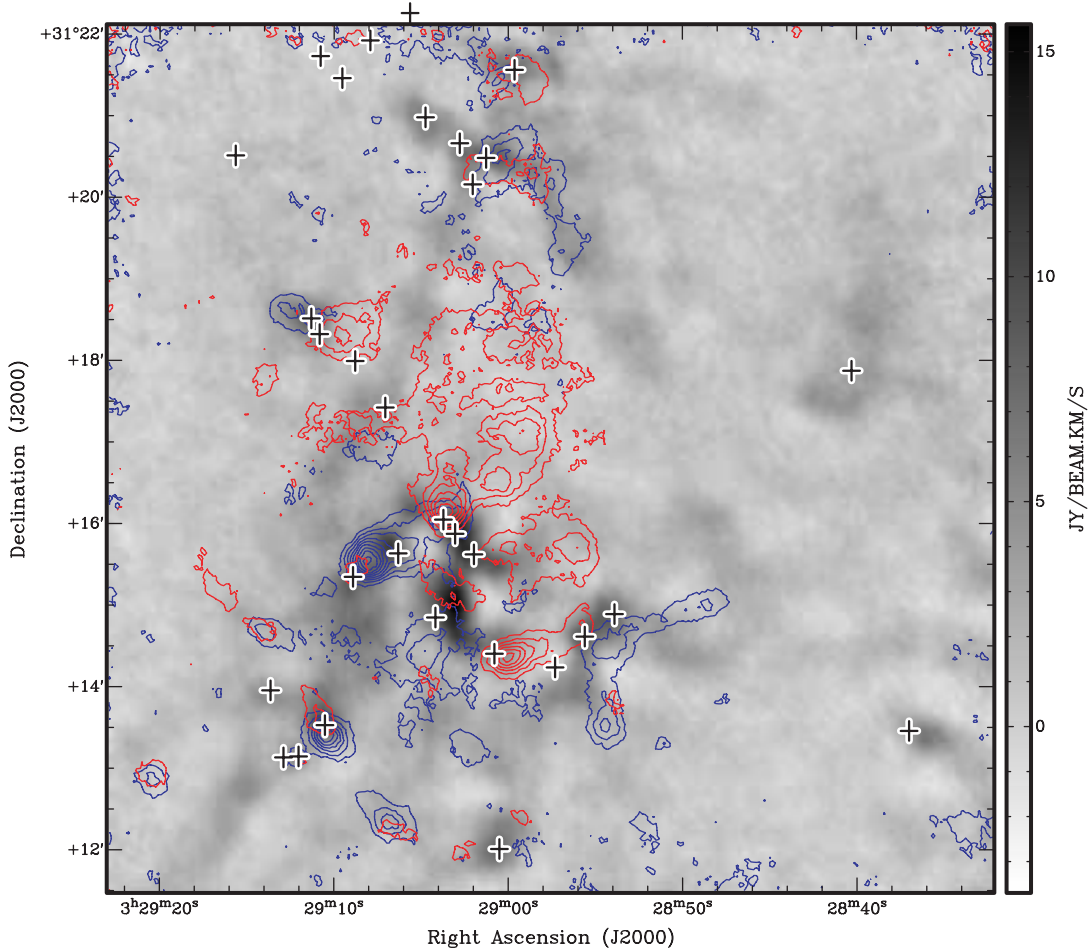


FIG. 5.— HCO^+ outflows in NGC 1333. The gray scale is N_2H^+ integrated intensity. Blue contours represent HCO^+ integrated emission from -5.5 to $+5.3 \text{ km s}^{-1}$. Red contours represent HCO^+ integrated emission from 10.4 to 16.4 km s^{-1} . The lowest contour (both red and blue) is at 9 Jy beam^{-1} and increase in steps of 4 Jy beam^{-1} to a maximum of 33 Jy beam^{-1} for the red and 41 Jy beam^{-1} for the blue.

We chose to identify cores using the default setting of searching down to twice the rms noise level, with spacing between contours also twice the rms noise ($0.244 \text{ Jy beam}^{-1}$). We require that each core must contain at least enough pixels to fill 1 beam. We found that sometimes CLUMPFIND was inadequate for separating out multiple cores. For example, Figure 6 shows a small portion of one velocity channel of the N_2H^+ data cube, with identified cores shaded differently. The contours are the N_2H^+ emission and coincide with the contours used by CLUMPFIND to identify cores. Three cores are identified by CLUMPFIND in this region. However, CLUMPFIND failed to break up the largest core along the line shown. We believe that cores like this should be divided because there are closed contours on both sides of the dividing line. In this case, we divide the core into two by running CLUMPFIND again with a smaller separation of contours. In this manner we have avoided limitations of the CLUMPFIND program and we believe we have separated cores in an unbiased manner. Note that while the smallest identified clump, to the south with the darkest shading, appears to show two closed contours, the smaller peak contains less than the required number of pixels to fill a beam. Therefore, it is not assigned to be a separate core.

Many of the weakest cores identified by CLUMPFIND were found to be noise spikes. We therefore employed a reality check on all clumps. Because we have data on all seven hyperfine components of the N_2H^+ line, we checked the N_2H^+ spectrum of the

core to make sure all seven components were visible. This is a very robust test because we identified our cores on a weak hyperfine component and so it was easy to discern a noise spike from a true N_2H^+ core. Furthermore, we checked that the morphology of the core identified in the isolated hyperfine component was similar to that seen in the brighter hyperfine components. As a result we have identified 93 cores.

The details of the cores are shown in Table 1 and their relative positions are shown in Figure 7. As mentioned previously, there are five dust continuum cores to the northeast (SK01) that do not exhibit any N_2H^+ emission. Apart from these, nearly every SK01 continuum core coincides with an N_2H^+ core. The only exception is core 17 from SK01, located to the southwest of IRAS 6, which also does not show any N_2H^+ emission. Figure 8 shows example N_2H^+ and HCO^+ spectra for two cores (27 and 85), which are examples of high- and low-mass cores, respectively. It is clear that the N_2H^+ emission toward core 85 (the lower mass core) is well detected. As can be seen in Figure 7, many of the cores are found in filamentary structures of high aspect ratio. These filaments are seen extending to the southeast and southwest of IRAS 6 and to the southeast of SSV 13, through IRAS 4. The filaments appear to closely (but not exactly) follow the dust distribution (SK01). We also calculate the core mass by two different methods: the LTE approximation and by using the virial theorem. These are discussed in detail in the following sections.

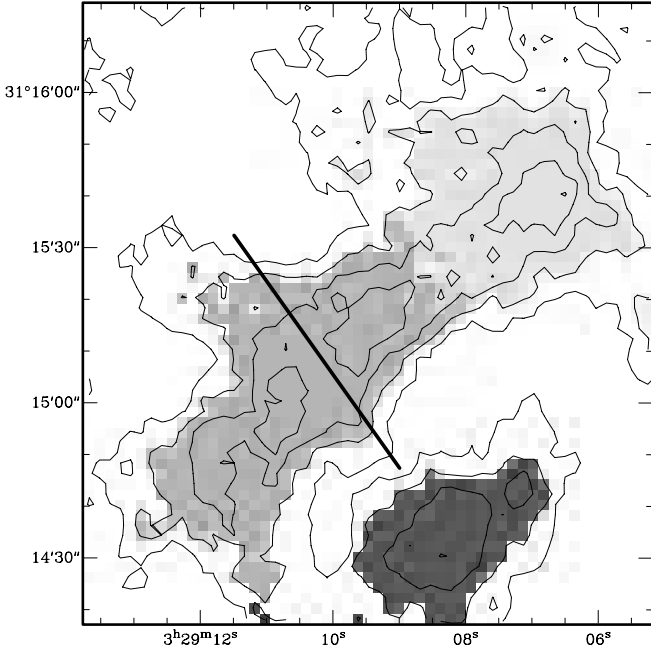


FIG. 6.—CLUMPFIND results for a small portion of the N_2H^+ data cube. The different shadings represent the identified cores. The contours are N_2H^+ emission at the same levels as those used by CLUMPFIND: 0.244, 0.488, 0.732, ..., 2.196 Jy beam $^{-1}$. The diagonal line represents an artificial break in the largest core that should be applied to separate this core into two individual cores.

4.1.1. LTE Mass

We assume that the column density traced by the $\text{N}_2\text{H}^+(1-0)$ transition in a core is given by (Williams et al. 1994)

$$N = \frac{3\epsilon_0 k}{\pi^2 \nu \mu^2} \left(1 - e^{-h\nu/kT}\right)^{-1} \left(\frac{T}{J(T) - J[2.73]}\right) \int T(v) dv, \quad (1)$$

where

$$J(T) = \frac{h\nu}{k(e^{h\nu/kT} - 1)}, \quad (2)$$

where ϵ_0 is the permittivity of free space, μ is the dipole moment for $\text{N}_2\text{H}^+(1-0)$, which is 3.4 D (1.13×10^{-29} C m), and $\int T(v) dv$ is the line integrated intensity. We assume the temperature of the gas (T) to be 15 K. We choose 15 K because it is on the upper limits for temperatures of isolated cores (Benson & Myers 1989), and we expect temperatures to be slightly higher in clustered regions. However, we caution that uncertainties in temperature may lead to an error as large as a factor of a few. To convert this to a hydrogen column density, we assume the relative abundance of N_2H^+ is 1.8×10^{-10} . We find values quoted in the literature from 3×10^{-11} (Bergin et al. 2002) for the isolated core B68 to 5×10^{-9} for IRAS 2 in NGC 1333 (Jørgensen et al. 2004a), which both appear to be extreme cases. Reasons for assuming this abundance are given in § 4.1.3, but we note here that our assumed relative abundance lies within the extremes and will be a representative value for most cases, although we might expect deviations of up to an order of magnitude in extreme situations. Thus, the hydrogen column density is given by

$$N_{\text{H}} = 9 \times \frac{N}{1.8 \times 10^{-10}}. \quad (3)$$

The factor of 9.0 in the above equation is determined by measuring the average ratio of the flux of the isolated N_2H^+ hyperfine component to the total flux, and assumes the line is optically thin. The LTE mass is then calculated using

$$\left(\frac{M_{\text{LTE}}}{M_{\odot}}\right) = 3.756 \times 10^{-32} \times \bar{m} \left(\frac{N_{\text{H}_2}}{\text{m}^{-2}}\right) \left(\frac{T_{\text{av}}}{\text{K}}\right) \left(\frac{d}{\text{pc}}\right)^2 \left(\frac{\text{pixsize}}{\text{arcsec}}\right)^2 \left(\frac{\Delta V}{\text{km s}^{-1}}\right) N_{\text{PIX}}, \quad (4)$$

where \bar{m} is the mean molecular weight of the gas, taken to be 2.3; N_{H_2} is taken from equation (3) above and assumes the gas is molecular; T_{av} is the mean brightness temperature of each pixel of the core identified by CLUMPFIND; d is the distance to NGC 1333, which is taken to be 300 pc (de Zeeuw et al. 1999; Belikov et al. 2002); pixsize is the size of the data cube pixels in arcseconds, which is $2''$ for our data; ΔV is the velocity width of each channel, 0.157 km s^{-1} ; N_{PIX} is the number of pixels that are identified with the core.

The uncertainty in the calibration of our flux density scale will contribute an error to the derived LTE masses. We estimate this error to be no greater than 20%. Our assumed distance of 300 pc comes from *Hipparcos* measurements; however, we note distances in the literature ranging from 220 (SK01) to 350 pc (Di Francesco et al. 2001). Thus, masses and sizes will need adjusting when comparing to work using different distances. We also anticipate that uncertainty in the temperature of the gas (we assume 15 K) will also contribute an error which may be as large as a factor of a few. We believe the error associated with the uncertainty in the relative abundance of N_2H^+ to be the largest error in the LTE mass calculation.

4.1.2. Virial Mass

We can also use the N_2H^+ data to calculate virial masses for the cores with

$$M_{\text{VIR}} = 210 \delta V^2 r, \quad (5)$$

where δV is the line FWHM and r is the effective radius of the core (col. [5] of Table 1) (Caselli et al. 2002). Equation (5) assumes a uniform density profile. If we assume a density profile that falls off as r^{-2} , then the constant 210 in equation (5) changes to 126 (Williams et al. 1994). Thus, our calculation of the virial mass of the cores may decrease by a factor of 2. We also note that the virial mass ignores magnetic fields, as well as the effects of an external pressure, which may have a significant effect on the virial mass in a region such as NGC 1333, due to mechanical pressure from outflows impinging on the cores. Furthermore, outflows are likely to be hot, which also may increase the pressure on the cores.

4.1.3. Comparison of M_{LTE} and M_{VIR}

The LTE mass is a measure of the amount of matter located within a core, whereas the virial mass is a measure of amount of matter required to keep a core bound. Therefore, we can compare the two masses to evaluate whether a core has enough self gravity to stay bound or not. If a core is bound, then the LTE mass should be greater than or equal to the virial mass. The distribution of virial masses with respect to LTE masses for the same core is shown in Figure 9. We have chosen a value of the N_2H^+ relative abundance (1.8×10^{-10}) such that the points in Figure 9 are distributed evenly about the line of equality ($M_{\text{LTE}} = M_{\text{VIR}}$), shown by the solid line. If we assume a different relative abundance, then this will have the effect of sliding the diagonal line of equality along

TABLE 1
N₂H⁺ CORE PROPERTIES

CORE NUMBER (1)	POSITION (J2000.0)		PEAK VELOCITY (km s ⁻¹) (4)	RADIUS (pc) (5)	LINE WIDTH (km s ⁻¹) (6)	LTE MASS (M _⊙) (7)	VIRIAL MASS (M _⊙) (8)
	R.A. (2)	Decl. (3)					
01.....	03 29 02.6	+31 14 56	7.80	0.02	0.62	2	2
02.....	03 29 03.7	+31 15 00	7.17	0.02	0.34	1	0.5
03.....	03 29 03.2	+31 15 18	7.64	0.02	0.54	2	1
04.....	03 29 02.4	+31 15 46	8.12	0.02	0.61	2	2
05.....	03 29 02.6	+31 15 54	8.27	0.03	0.70	2	3
06.....	03 29 00.7	+31 15 32	8.43	0.02	0.64	1	2
07.....	03 29 06.8	+31 15 44	8.12	0.03	0.70	3	3
08.....	03 29 00.4	+31 12 04	7.17	0.02	0.58	2	1
09.....	03 29 00.1	+31 12 18	7.17	0.02	0.56	1	1
10.....	03 29 02.9	+31 11 44	7.33	0.005	0.20	0.06	0.08
11.....	03 28 55.9	+31 14 16	7.33	0.03	0.56	2	2
12.....	03 28 57.0	+31 13 56	7.02	0.03	0.39	1	1
13.....	03 28 54.3	+31 14 46	7.17	0.02	0.55	1	1
14.....	03 29 04.9	+31 20 58	7.64	0.02	0.52	1	1
15.....	03 29 11.8	+31 18 30	8.43	0.03	0.50	2	2
16.....	03 29 05.4	+31 16 12	8.43	0.01	0.31	0.4	0.2
17.....	03 29 01.8	+31 14 36	6.55	0.02	0.61	1	2
18.....	03 29 04.2	+31 14 48	6.70	0.02	0.37	0.9	0.6
19.....	03 29 07.8	+31 14 50	7.02	0.03	0.41	1	1
20.....	03 28 36.2	+31 13 24	7.33	0.01	0.34	0.7	0.2
21.....	03 29 08.4	+31 15 02	7.17	0.01	0.21	0.3	0.09
22.....	03 29 09.0	+31 15 10	7.33	0.02	0.59	2	2
23.....	03 29 10.7	+31 15 02	7.80	0.02	0.32	0.9	0.4
24.....	03 29 08.8	+31 14 44	7.49	0.02	0.37	1	0.6
25.....	03 28 35.1	+31 13 20	7.64	0.02	0.48	0.6	1
26.....	03 29 02.3	+31 20 30	7.80	0.02	0.61	2	2
27.....	03 28 59.6	+31 21 36	7.64	0.02	0.56	1	1
28.....	03 29 13.1	+31 13 54	7.80	0.02	0.44	1	0.8
29.....	03 29 10.7	+31 13 52	7.64	0.01	0.51	0.7	0.6
30.....	03 28 40.3	+31 17 40	7.80	0.03	0.42	2	1
31.....	03 28 42.2	+31 17 32	8.12	0.02	0.39	0.6	0.6
32.....	03 28 55.3	+31 19 16	7.80	0.02	0.45	0.8	0.9
33.....	03 29 00.6	+31 20 26	7.96	0.01	0.55	0.8	0.6
34.....	03 28 59.2	+31 20 22	7.64	0.01	0.31	0.3	0.2
35.....	03 28 39.4	+31 18 28	8.12	0.02	0.44	1	0.8
36.....	03 28 53.9	+31 14 54	8.27	0.01	0.41	0.6	0.4
37.....	03 29 10.4	+31 13 34	7.17	0.01	0.70	0.7	1
38.....	03 29 11.8	+31 13 08	6.86	0.02	0.58	0.5	1
39.....	03 29 08.4	+31 14 02	6.86	0.01	0.29	0.2	0.2
40.....	03 29 07.8	+31 14 10	6.86	0.01	0.33	0.3	0.2
41.....	03 28 53.9	+31 12 58	7.02	0.01	0.41	0.7	0.4
42.....	03 29 14.9	+31 12 44	7.33	0.01	0.44	0.6	0.4
43.....	03 29 12.6	+31 13 14	7.33	0.01	0.29	0.4	0.2
44.....	03 29 09.0	+31 14 10	7.17	0.01	0.22	0.2	0.1
45.....	03 29 08.4	+31 14 12	7.17	0.01	0.29	0.1	0.2
46.....	03 29 16.5	+31 12 06	7.49	0.01	0.26	0.1	0.1
47.....	03 29 15.7	+31 12 32	7.49	0.01	0.33	0.2	0.2
48.....	03 29 13.8	+31 13 14	7.49	0.02	0.34	0.4	0.5
49.....	03 29 09.0	+31 14 10	7.17	0.01	0.22	0.2	0.1
50.....	03 28 49.7	+31 14 30	7.49	0.02	0.44	0.4	0.8
51.....	03 28 51.1	+31 14 30	7.64	0.01	0.35	0.3	0.3
52.....	03 29 00.7	+31 15 26	7.49	0.01	0.21	0.3	0.09
53.....	03 29 00.0	+31 20 54	7.49	0.02	0.25	0.4	0.3
54.....	03 28 51.8	+31 15 34	7.64	0.01	0.27	0.3	0.2
55.....	03 28 58.7	+31 15 44	7.64	0.01	0.22	0.2	0.1
56.....	03 28 53.6	+31 18 24	7.64	0.03	0.53	0.9	2
57.....	03 29 02.3	+31 19 52	7.64	0.02	0.36	0.4	0.5
58.....	03 29 04.0	+31 19 22	8.12	0.01	0.45	0.3	0.4
59.....	03 28 58.2	+31 20 58	7.64	0.01	0.29	0.3	0.2
60.....	03 28 47.3	+31 15 18	7.96	0.02	0.30	0.4	0.4
61.....	03 28 33.0	+31 15 28	7.96	0.01	0.40	0.1	0.3
62.....	03 28 49.2	+31 16 06	8.12	0.01	0.33	0.3	0.2

TABLE 1—*Continued*

CORE NUMBER (1)	POSITION (J2000.0)		PEAK VELOCITY (km s ⁻¹) (4)	RADIUS (pc) (5)	LINE WIDTH (km s ⁻¹) (6)	LTE MASS (M _⊙) (7)	VIRIAL MASS (M _⊙) (8)
	R.A. (2)	Decl. (3)					
63.....	03 28 47.9	+31 16 04	8.12	0.01	0.35	0.3	0.3
64.....	03 29 08.7	+31 17 32	8.27	0.02	0.37	0.5	0.6
65.....	03 29 09.3	+31 14 46	8.27	0.01	0.19	0.2	0.08
66.....	03 29 09.2	+31 16 54	8.27	0.02	0.38	0.7	0.6
67.....	03 29 08.7	+31 17 32	8.27	0.02	0.37	0.5	0.6
68.....	03 29 07.1	+31 17 28	8.43	0.02	0.43	0.5	0.8
69.....	03 29 04.8	+31 18 36	8.27	0.02	0.55	0.6	1
70.....	03 28 57.1	+31 22 04	8.59	0.01	0.40	0.2	0.3
71.....	03 29 03.2	+31 13 36	7.02	0.02	0.40	0.6	0.7
72.....	03 28 50.3	+31 11 34	7.02	0.003	0.36	0.05	0.3
73.....	03 29 09.9	+31 15 26	7.02	0.01	0.18	0.05	0.07
74.....	03 29 04.8	+31 11 56	7.17	0.005	0.17	0.05	0.06
75.....	03 29 04.2	+31 14 04	7.49	0.01	0.37	0.2	0.3
76.....	03 29 09.0	+31 21 06	7.33	0.01	0.28	0.08	0.2
77.....	03 29 06.3	+31 12 52	7.49	0.01	0.20	0.1	0.08
78.....	03 28 47.5	+31 14 24	7.64	0.007	0.23	0.2	0.1
79.....	03 28 50.9	+31 17 48	7.49	0.01	0.19	0.08	0.08
80.....	03 29 18.4	+31 11 42	7.64	0.01	0.16	0.08	0.05
81.....	03 28 59.6	+31 13 46	7.80	0.01	0.22	0.1	0.1
82.....	03 29 13.4	+31 14 36	7.64	0.01	0.30	0.1	0.2
83.....	03 28 50.6	+31 16 38	7.64	0.01	0.26	0.08	0.1
84.....	03 29 06.0	+31 16 42	8.12	0.02	0.34	0.4	0.5
85.....	03 28 42.0	+31 19 06	7.80	0.006	0.16	0.05	0.05
86.....	03 29 06.7	+31 19 50	7.96	0.006	0.17	0.05	0.06
87.....	03 28 33.6	+31 16 42	7.96	0.004	0.29	0.05	0.2
88.....	03 28 34.2	+31 16 46	7.96	0.01	0.33	0.2	0.2
89.....	03 28 38.0	+31 16 40	7.96	0.01	0.25	0.06	0.1
90.....	03 28 33.6	+31 15 40	8.27	0.01	0.16	0.08	0.05
91.....	03 28 37.2	+31 17 44	8.12	0.004	0.20	0.06	0.08
92.....	03 28 57.0	+31 19 42	8.27	0.01	0.32	0.1	0.2
93.....	03 28 50.7	+31 18 58	8.43	0.01	0.16	0.08	0.05

NOTE.—Units of right ascension are hours, minutes, and seconds, and units of declination are degrees, arcminutes, and arcseconds.

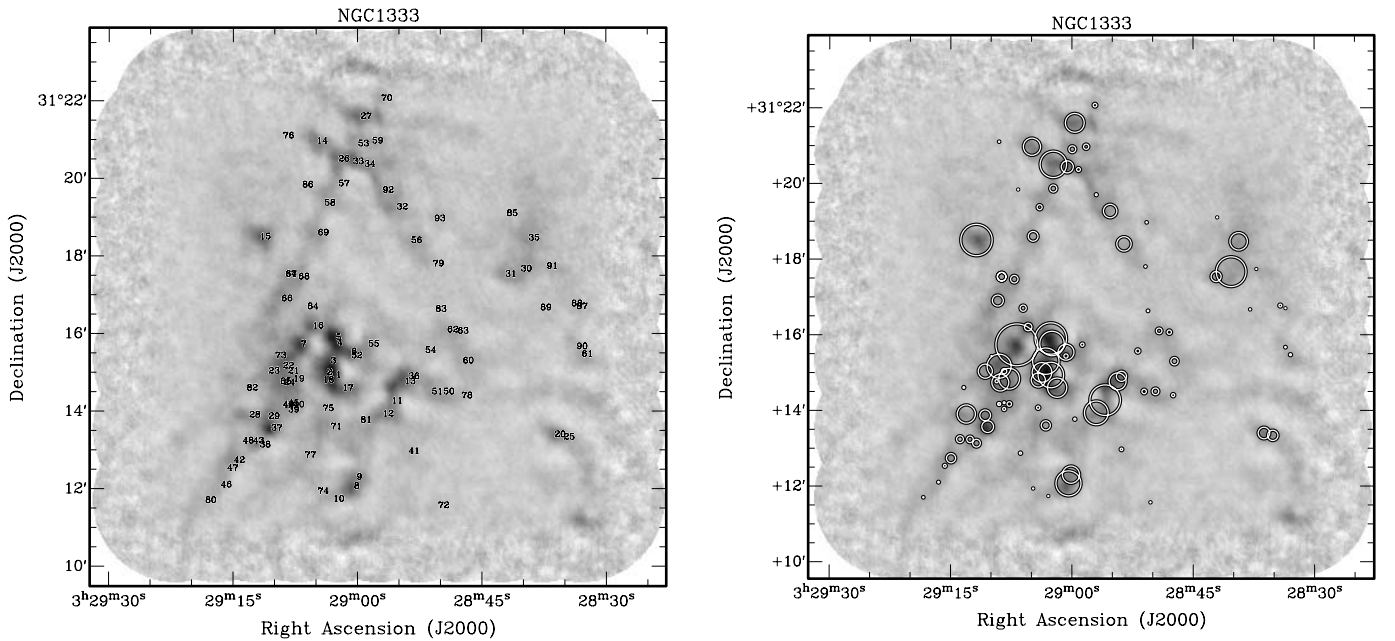


FIG. 7.—Distribution of identified N₂H⁺ cores. The gray scale is the N₂H⁺ integrated intensity map. Numbers on the left correspond to the positions of cores listed in Table 1. The radius of the rings on the right is proportional to the M_{LTE} for each core, listed in Table 1. Note: weak cores are seen on the edges of the map, which were not identified by CLUMPFIND as they lie outside the fully sampled region of the BIMA observations. An example is located at $\alpha = 03^{\text{h}}28^{\text{m}}33.0^{\text{s}}$, $\delta = +31^{\circ}11'12''$.

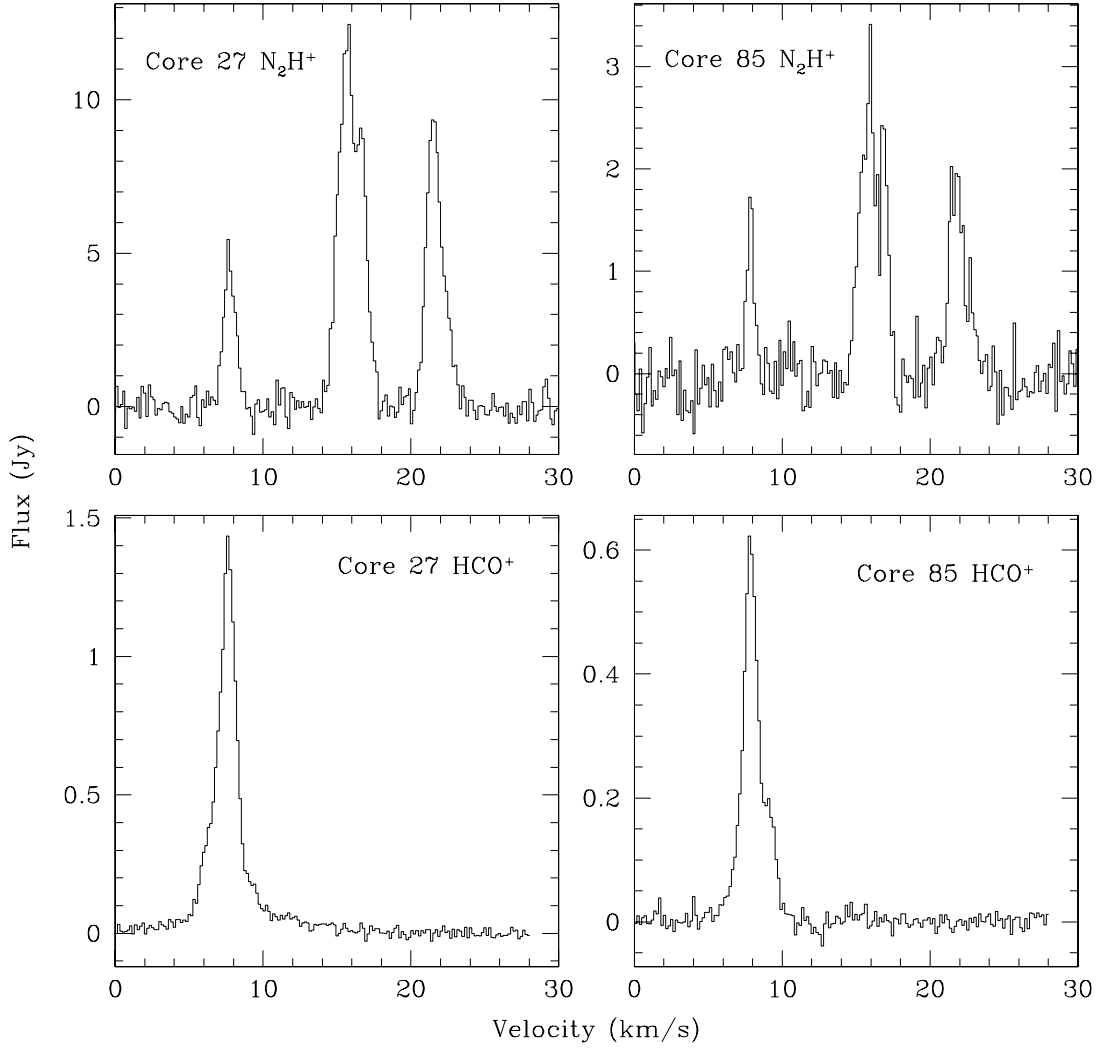


FIG. 8.— N_2H^+ and HCO^+ spectra for two example cores. The left-hand side shows N_2H^+ (top) and HCO^+ (bottom) spectra for core 27, which has an LTE mass of $1 M_\odot$. The right-hand side shows N_2H^+ (top) and HCO^+ (bottom) spectra for core 85, which has an LTE mass of $0.05 M_\odot$. In both cases the N_2H^+ emission is clearly detected, giving us confidence that each identified core is real.

the horizontal axis in Figure 9. Because of the uncertainty in the abundance, we cannot be sure whether individual cores are bound or unbound based solely on a comparison of their LTE and virial masses.

M_{VIR} and M_{LTE} are correlated with a correlation coefficient of 0.88 over a range in M_{LTE} of ~ 40 , despite the individual uncertainties in M_{VIR} and M_{LTE} . Such a correlation is unlikely to be a coincidence, suggesting that most of the cores are self-gravitating, at both high and low ends of the mass range. If proportionately more of the lowest mass cores were unbound, compared to the highest mass cores, then we would expect to see the distribution of points in Figure 9 to turn up toward the virial mass axis, in the lower left (lowest mass) corner. However, there are approximately equal numbers of points above (19) and below (18) the solid line with $M_{\text{LTE}} < 0.3$, as compared to approximately equal numbers of points above (29) and below (27) the solid line with $M_{\text{LTE}} > 0.3$. The curved line in Figure 9 is a second-order polynomial fit to the data points, given in equation (6):

$$\log(M_{\text{VIR}}) = 0.071 + 1.38 \log(M_{\text{LTE}}) + 0.26[\log(M_{\text{LTE}})]^2. \quad (6)$$

While the polynomial fit in Figure 9 does show a small turn-up at the lower mass end, the turn-up is small compared to the scatter in the data points. Therefore, we do not consider it significant. Thus, we have no evidence for such a turning up of the distribution in our data. We conclude that many of the lower mass cores are likely to be self-gravitating and are not transient objects.

Some of the higher mass cores can be expected to be bound, since they are associated with protostars, such as core 37 (IRAS 4A), core 38 (IRAS 4B), core 36 (IRAS 2C), and core 15 (IRAS 7). Below we detail some of the properties of these cores.

Core 37 (IRAS 4A).—We calculate an LTE mass of $0.7 M_\odot$ and a virial mass of $1.0 M_\odot$. This might suggest that the core is unbound, but we know this is not the case because IRAS 4A contains at least two protostars (Lay et al. 1995); an alternate explanation is needed. IRAS 4A was observed by Di Francesco et al. (2001) in N_2H^+ at a higher resolution than our observations. They calculate the LTE mass of IRAS 4A to be $0.73 M_\odot$, assuming the distance to NGC 1333 is 350 pc and $X(\text{N}_2\text{H}^+) = 6.0 \times 10^{-11}$. Converting this mass using our preferred distance (300 pc) and N_2H^+ relative abundance (1.8×10^{-10}), this is equivalent to $0.18 M_\odot$, a factor of 4 lower than our derived value. This is partly because their higher resolution observations filtered out

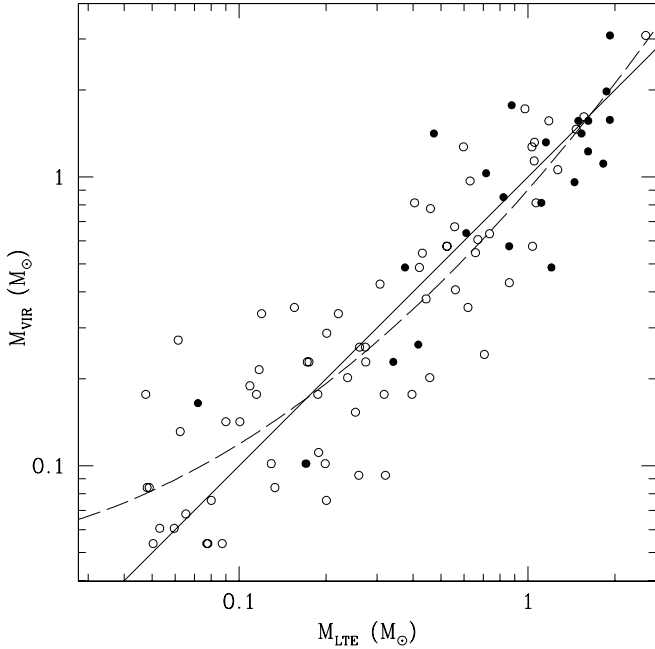


FIG. 9.—Distribution of core LTE and virial masses. Filled circles represent cores associated with stars, as detected by *Spitzer*, and open circles represent cores not associated with stars. The solid diagonal line represents equality between M_{LTE} and M_{VIR} , assuming an N_2H^+ relative abundance of 1.8×10^{-10} . The dashed curve represents a best fit to the data of the form $y = a + bx + cx^2$, where x is $\log(M_{\text{LTE}})$, y is $\log(M_{\text{VIR}})$, a is 0.071, b is 1.38, and c is 0.26.

some of the extended emission. By combining the BIMA data with the FCRAO data, we have minimized this problem. The relative abundance of N_2H^+ makes a significant difference to the derived LTE mass. We can check our derived relative abundance by comparing LTE mass to that derived from dust continuum measurements by SK01. SK01 determine the mass of IRAS 4A to be $1.5 M_\odot$, assuming a distance of 220 pc. To reproduce our LTE mass, we require a relative abundance of 5×10^{-11} , similar to that derived by Di Francesco et al. (2001). Therefore, we agree with the finding of Di Francesco et al. (2001) that there is an unusually low relative abundance of N_2H^+ at IRAS 4A. We see the effect of this lowered abundance when comparing the relative intensities of N_2H^+ and $850 \mu\text{m}$ continuum emission at IRAS 4A in Figure 3. The continuum contours strongly peak at the position of IRAS 4A while the N_2H^+ emission is only a weak peak at this position.

A possible explanation for the low abundance is that IRAS 4A is the source of an outflow, which is traced by HCO^+ . The HCO^+ , and CO, will be enhanced in the gas phase by the shocks from the outflow. Since both HCO^+ and CO destroy N_2H^+ (Jørgensen et al. 2004b), we expect to find a lower N_2H^+ abundance here. An alternate explanation is that IRAS 4A has undergone thermal processing of its N_2H^+ , thereby reducing the N_2H^+ abundance.

Core 38 (IRAS 4B).—We calculate an LTE mass of $0.5 M_\odot$ and a virial mass of $1.4 M_\odot$. Again, this might imply the core is unbound, but we know this is not the case (Lay et al. 1995). Di Francesco et al. (2001) have also observed this core at higher resolution and find an LTE mass of $0.41 M_\odot$, using the same assumptions as for IRAS 4A. Here, we assume that again there is a significant amount (a factor of 5) of missing N_2H^+ flux in the data of Di Francesco et al. (2001). Comparing our LTE calculations to the dust continuum mass derived by SK01, we can estimate the relative N_2H^+ abundance. SK01 derive a combined mass of $0.63 M_\odot$ for IRAS 4B west and east. We combine the masses

for the west and east components here because our resolution was not high enough for CLUMPFIND to separate N_2H^+ emission surrounding the two protostars. The N_2H^+ abundance is then estimated to be 1×10^{-10} , close to assumed abundance of 1.8×10^{-10} .

Core 36 (IRAS 2C).—We calculate an LTE mass of $0.6 M_\odot$ and a virial mass of $0.4 M_\odot$. IRAS 2C has been identified as one of the youngest sources in NGC 1333 and is most likely a Class 0 source (SK01). SK01 also use their dust continuum observations to derive a mass of $0.05 M_\odot$. In this case, it appears there is an N_2H^+ abundance enhancement of about 6 over the assumed average value.

Core 15 (IRAS 7).—We calculate an LTE mass of $2 M_\odot$ and a virial mass of $1.6 M_\odot$. SK01 calculate a mass of $0.16 M_\odot$ for the combined contributions of SM 1 and SM 2. Again, it appears the abundance may be enhanced by a factor of a few over the average value.

4.2. Association of Cores with Stellar Sources

Recent observations of NGC 1333 with the *Spitzer Space Telescope* (R. Gutermuth et al. 2006, in preparation) allow us to compare the incidence of our N_2H^+ cores with infrared stars. All the stars we correlate with N_2H^+ cores are known to be pre-main-sequence stars within NGC 1333, by nature of their infrared colors, using the bands at 3.6 , 4.5 , and $5.8 \mu\text{m}$, which identifies Class I, II, and III sources. In addition to this, we used 24 and $70 \mu\text{m}$ *Spitzer* images to associate cores with Class 0 sources. We note that all previously known Class 0 sources in the field of view are easily detected at these longer wavelengths. The infrared observations have a sensitivity limit of around $0.05 M_\odot$, which is similar to the mass limit of our detected cores. We consider a star associated with an N_2H^+ core if any part of the N_2H^+ core, as defined by CLUMPFIND, overlaps with the peak of the infrared emission.

Using the same association criteria, we have used a Monte Carlo simulation to test how many chance alignments of N_2H^+ cores and infrared sources we might expect. To do this, we assume an average N_2H^+ core size of 0.015 pc and randomly place 93 simulated cores in the field of view and count the number of chance alignments. This process is repeated to derive a distribution of expected chance alignments. From these simulations, we expect 3.5 chance alignments of N_2H^+ cores with infrared stars. This low number of chance alignments is unlikely to affect our results discussed below.

N_2H^+ cores with associated stars are shown in Figure 9. It is clear from this figure that N_2H^+ cores associated with stars tend to have higher masses than those without. This can also be seen in Figure 10, as well as the distributions of other attributes of the N_2H^+ cores. Both the distributions of N_2H^+ core LTE and virial masses are extremely unlikely to come from the same population. Figure 10 also shows that cores without associated stars are generally smaller than those with stars. Implications of this are discussed further in § 4.3.

The N_2H^+ core line FWHM is generally smaller for cores not associated with stars. This is what would be expected if the stars are active in creating local turbulence through their stellar winds and outflows. Such winds and outflows should stir up the immediate environment of surrounding gas, increasing the measured line FWHM. The tendency of cores with associated stars to have larger line widths has been seen in ammonia cores (Benson & Myers 1989; Jijina et al. 1999).

4.3. Mass Distribution of the Cores

Recent simulations by Bonnell et al. (2001b) and Bate & Bonnell (2005) indicate that the initial mass function (IMF) is created at an advanced stage of evolution. Initially all cores start

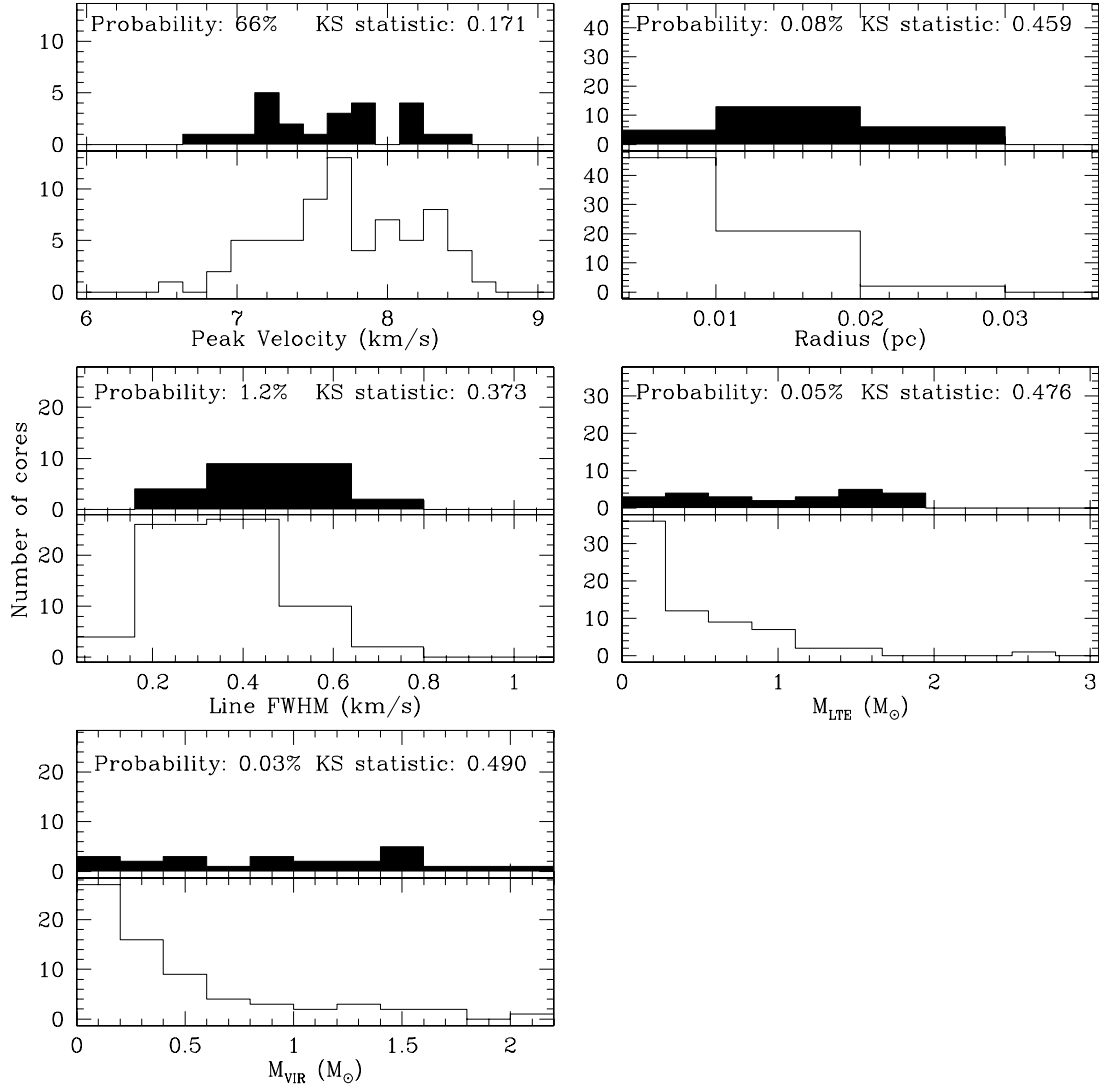


FIG. 10.—Distributions of N₂H⁺ core parameters depending on whether they are associated with stars (*filled histograms*) or not (*open histograms*). For each pair of distributions, a Kolmogorov-Smirnov (K-S) test is applied and the resulting K-S statistic and probability is given. This is the probability that the two distributions are drawn from the same sample. Significant differences are seen in all distributions except peak velocity.

with the same mass, which is determined by the opacity limit for fragmentation. Stars build up their mass through accretion. The final mass of the star is then determined by stochastic ejection of the stars from the cluster due to dynamical interactions. However, previous observations of prestellar dust cores in the ρ Ophiuchi main cloud (Motte et al. 1998; Johnstone et al. 2000) show that the mass distribution of some of the prestellar cores resembles the IMF. This suggests that the IMF may be locked in at the prestellar stage, in contradiction to the simulations. The previous observations by Motte et al. (1998) and Johnstone et al. (2000) were continuum measurements and so no line width information for the cores is known. It is therefore possible that the prestellar cores are transient phenomena and may not form stars, as suggested by Ballesteros-Paredes & Mac Low (2002). Our N₂H⁺ data have shown that in NGC 1333 at least, the N₂H⁺ cores appear to be close to virialized and therefore a significant proportion are likely to be bound and are therefore more likely to form stars.

In Figure 11 we show the distribution of core LTE and virial masses. The LTE and virial mass distributions are very similar. Furthermore, we find these distributions similar to the average

field star IMF, although the LTE and virial mass distributions do not show a decrease for lower mass cores, as is seen in the IMF.

Such similarities between the stellar IMF and the mass function of dust cores has also been found by Motte et al. (1998), Johnstone et al. (2000), and Stanke et al. (2006), who suggested this is evidence that the IMF may be locked in at this early stage of star formation. A problem with comparing the mass function of dust cores and stars is that it is not clear whether the dust cores are bound or not—no information on their internal motions is known. The N₂H⁺ data allow us to overcome this problem. If the N₂H⁺ cores are bound regardless of mass, this suggests that such emission does not trace transient structures formed out of turbulent fluctuations. Therefore, this implies the entire mass distribution consists of objects that may potentially form stars.

It is interesting to note that in Figure 10 we see a flat distribution of core masses (both LTE and virial) for those cores associated with stars. This flat distribution is clearly unlike the field star IMF. There appear to be too few low-mass cores to form a mass function similar to the field star IMF. Because both the N₂H⁺ and infrared observations have a sensitivity limit of around $0.05 M_{\odot}$, we do not believe this is an effect of the sensitivity limits.

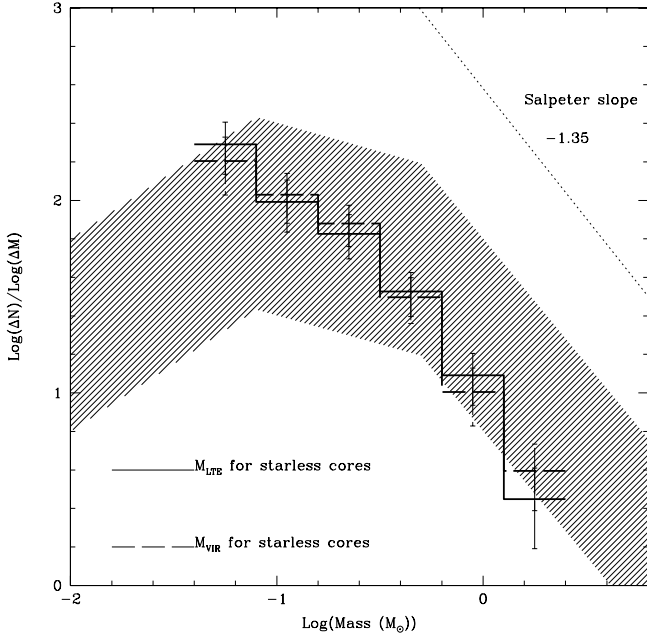


FIG. 11.—Distribution of starless core LTE and virial masses derived from the N_2H^+ data. The solid line histogram shows the LTE masses and the dashed line histogram shows the virial masses, with error bars representing \sqrt{N} statistics. The LTE masses were determined, assuming a relative abundance of 1.8×10^{-10} for N_2H^+ . The shaded area represents the average field star IMF, with uncertainty, as determined by Kroupa (2002). The dotted diagonal line represents the Salpeter IMF slope (Salpeter 1955). Both the starless core LTE and virial masses are consistent with the field star IMF, given the error bars represented by the shaded area.

As a core forms a star, it loses gas mass. If lower mass cores lose a bigger proportion of their mass than do higher mass cores, the lower mass cores move left in the distribution shown in Figure 10 more than the higher mass cores, making the mass function distribution shallower. But if more of the high mass cores make multiple stars than do low-mass cores, the mass function should look steeper. These are two competing effects that may well affect the distribution we see. Future research should be undertaken to identify the cause of this apparent flattening of the mass function.

4.4. Clustering

NGC 1333 is known as a region of clustered star formation (Aspin et al. 1994; Lada et al. 1996). As can be seen from Figure 7, the N_2H^+ cores also appear to cluster, showing a concentration in the IRAS 4/IRAS 2/SSV 13 region, with a particular concentration of cores around SSV 13. In Figure 12 we show a comparison of clustering properties of N_2H^+ cores for varying LTE masses. For each core, the upper plot shows the number of cores that are within a radius of 0.2 pc, while the lower plot shows how far away the nearest core is. Both distributions are a measure of the clustering properties of the cores throughout their mass spectrum. As can be seen, there is no clear correlation between either of the distributions. However, it appears that only a small proportion of cores with $M < 0.2 M_\odot$ have more than four neighbors (43%), whereas proportionately more of the higher mass cores have more than four neighbors (79%). But this trend is weak and does not appear for other choices mass cutoff. This implies that there is little significant increase in the likelihood of finding a more massive core in a clustered region, than a lower mass core. Furthermore, when cores are separated into those that are associated with stars (*filled circles*) and those that are not (*open circles*), there is no significant difference between the two populations.

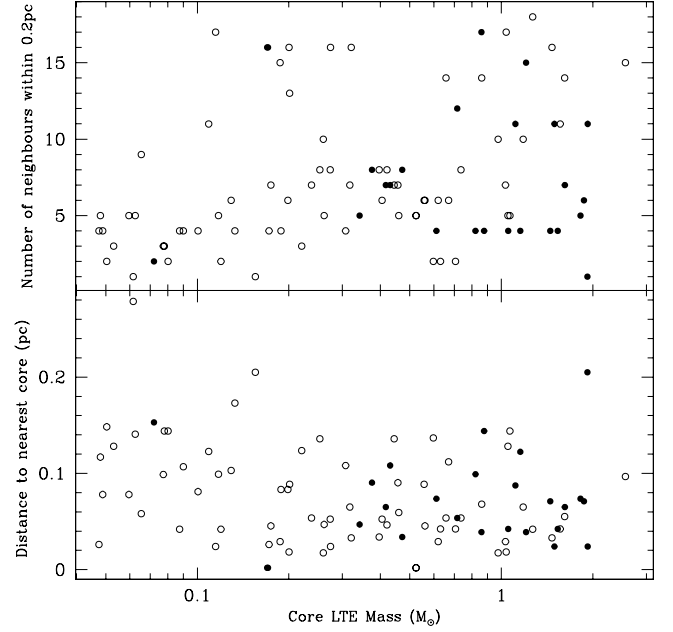


FIG. 12.—Distribution of clustering properties for N_2H^+ cores. The upper plot shows the number of cores within 0.2 pc of each core. The lower plot shows the distance to the nearest core. Filled circles represent those cores that are associated with stars. Open circles represent cores that are not associated with stars. Both plots show that there is no correlation between the clustering properties of cores with high or low mass.

4.5. Motions of the Cores

An important difference between isolated and clustered star formation is the effects of turbulence, which are expected to be larger in the clustered environment. Di Francesco et al. (2004) have studied the relative motions of cores in the Ophiuchus A cluster region. The Oph A observations have a higher spatial resolution ($10'' \times 6''$, corresponding to 1250×750 AU) than the NGC 1333 observations ($10'' \times 10''$, corresponding to 3000 AU) but cover a smaller area (~ 0.1 pc for Oph A and ~ 1.0 pc for NGC 1333). Di Francesco et al. (2004) found little dispersion between the line-of-sight velocities of the cores they detected within Oph A with an rms dispersion of only 0.17 km s^{-1} . For NGC 1333, we find a mean line-of-sight velocity of 7.66 km s^{-1} and an rms dispersion of 0.46 km s^{-1} . This is larger than that found for Oph A. Examination of the N_2H^+ data cube suggests that this is because there appear to be two regions of N_2H^+ emission along the same line of sight in the vicinity of SSV 13. These are traced by cores 4, 5, 6, 7, 16, and 84, which all have velocities greater than 8.1 km s^{-1} , and cores 1, 2, 3, 17, 18, 52, and 55, which all have velocities less than 7.8 km s^{-1} . For each velocity component, we find the rms dispersion is 0.14 and 0.34 km s^{-1} for cores greater than 8.1 and less than 7.8 km s^{-1} , respectively. Thus, it appears the velocity dispersion is larger in NGC 1333 than in Oph A, even taking into account the multiple velocity components along the line of sight in NGC 1333. For the N_2H^+ core line widths, we find an average value of 0.38 km s^{-1} and an rms dispersion of 0.14 km s^{-1} . These numbers are very similar to those found by Di Francesco et al. (2004) in Oph A: 0.39 and 0.11 km s^{-1} , respectively. So it appears that individual core kinematic properties are similar in Oph A and NGC 1333, but there are larger relative motions of the cores in NGC 1333. However, this may be an effect for measuring a much larger area in NGC 1333. In order to compare the two clusters in more detail, more cores need to be identified on a similar size scale to the Oph A observations.

We can investigate the motions of cores within the filamentary structures to the southeast of SSE 13 and to the southwest and southeast of IRAS 6. If we assume that the filamentary structures are true filaments; i.e., that they will also appear as filaments when observed orthogonal to the current viewing angle, then we can estimate how long it will take for cores to move the length of a filament, based on the observed velocity dispersion. This will tell us the typical timescale we might expect the filaments to survive. We find velocity dispersions of cores within the filament to the southeast of SSV 13 (0.6 pc long), and to the southwest (0.5 pc long) and southeast (0.5 pc long) of IRAS 6 to be 0.23, 0.27, and 0.24 km s^{-1} , respectively. Taking an average of 0.25 km s^{-1} , and assuming cores must travel 0.5 pc for a filament to dissipate, we calculate the filaments may survive for 2×10^6 yr. Such a long time implies these filaments may well be stable features.

Previously, Walsh et al. (2004) have investigated the relative motion of star forming cores with respect to their surrounding envelopes. This was done by observing $\text{N}_2\text{H}^+(1-0)$, which traces the high-density core motions and $^{13}\text{CO}(1-0)$ and $\text{C}^{18}\text{O}(1-0)$, which trace the low-density surroundings. They found little evidence for any ballistic relative motions. This is in contradiction to previous theoretical work (Bonnell et al. 1997, 2001a) that suggested that a star's final mass was determined by its motion through its natal cloud. The observations of Walsh et al. (2004) were focused mainly toward regions of isolated star formation, with a very small number of regions close to clustered environments. Their results were clear for the case of the isolated regions of star formation, but inconclusive for the clustered regions. With these new data, we are able to look for relative motions in NGC 1333 and thus extend the work to include a clustered region of star formation.

We use the line center velocities of the N_2H^+ cores given in Table 1 as our high-density tracer and the $^{13}\text{CO}(1-0)$ and $\text{C}^{18}\text{O}(1-0)$ FCRAO maps of Ridge et al. (2003) covering NGC 1333 as the low-density tracers. We determine the difference in line center velocities by using the N_2H^+ core velocities given in Table 1 and fitting a Gaussian to the ^{13}CO and C^{18}O line profiles of the spectrum that coincides with the peak of the N_2H^+ core. Not all N_2H^+ cores could be included in the analysis. This is because some of the CO spectra were too confused to reliably determine a relevant line center velocity. Figure 13 shows the difference in the line center velocities, which can be compared to Figure 1 of Walsh et al. (2004) for the case of isolated cores.

The top of Figure 13 shows simulated line profiles for the average line width of N_2H^+ , ^{13}CO , and C^{18}O . As previously discussed by Walsh et al. (2004), if we expect there to be no motions of the high-density cores with respect to their surroundings, then we would expect to see line center velocity differences distributed like the line profile for the N_2H^+ transition. If there are significant motions of the core, then we would expect to see broader distributions resembling the CO line profiles. Figure 13 shows that line center velocity differences have a distribution somewhere between these two extremes: The rms difference between N_2H^+ and ^{13}CO is 0.57 km s^{-1} and between N_2H^+ and C^{18}O is 0.53 km s^{-1} . These numbers can be compared to the average ^{13}CO FWHM of 1.18 km s^{-1} , average C^{18}O FWHM of 1.00 km s^{-1} and average N_2H^+ FWHM of 0.38 km s^{-1} . Unfortunately, our results may suffer from some errors that were avoided by Walsh et al. (2004). This is because we are using different telescopes, and observations were made under different conditions. One of the greatest source of errors is that our BIMA N_2H^+ data are of much higher spatial resolution than the FCRAO CO data. Thus, it is likely that the CO data trace somewhat different columns, compared to the N_2H^+ data. This will give an apparent increase in the differences of measured line center ve-

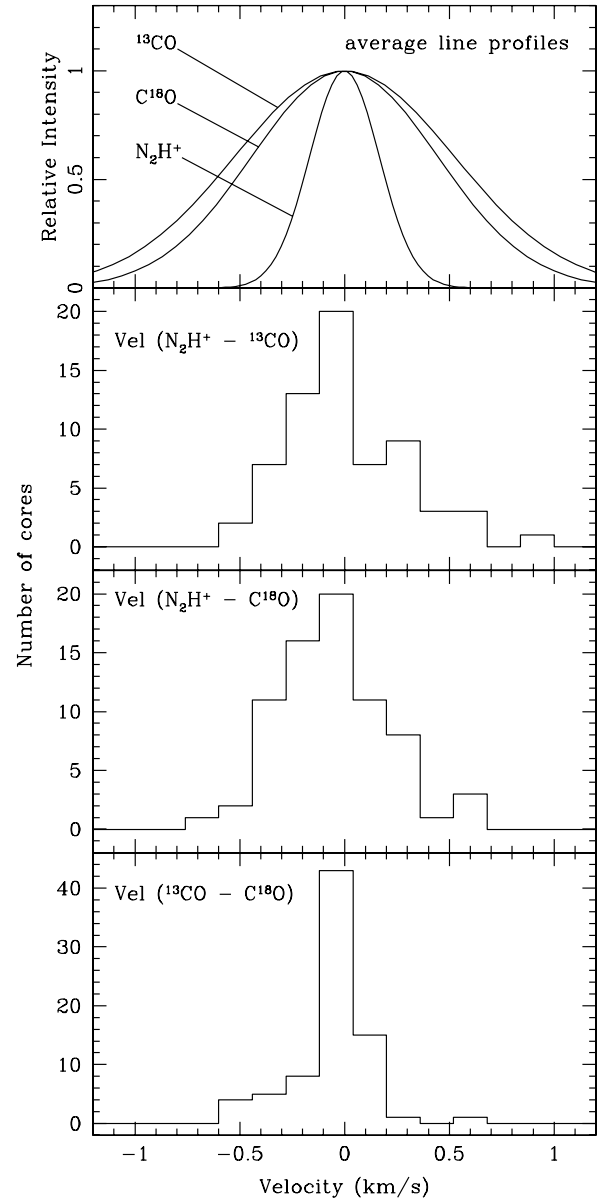


FIG. 13.—Line center velocity differences for N_2H^+ , ^{13}CO , and C^{18}O (bottom three plots). The top plot shows simulated line profiles of the three transitions, based on their average line profiles.

locities between N_2H^+ and the CO isotopes. This has the effect of rendering our results uncertain as to whether we can tell if there are relative motions of the cores, although we note that it seems to be consistent with the cores not moving ballistically. In order to obtain a clear answer, it will be necessary to obtain CO data with the same resolution as the N_2H^+ data, which is beyond the scope of this work.

5. SUMMARY AND CONCLUSIONS

We have used both the BIMA and FCRAO radio telescopes to observe $\text{HCO}^+(1-0)$ and $\text{N}_2\text{H}^+(1-0)$ in the clustered star forming region NGC 1333. Comparison with submillimeter continuum images shows that the N_2H^+ emission very closely follows the dust continuum, showing it is an excellent tracer of quiescent gas. HCO^+ , on the other hand, shows overall similarities with dust continuum but appears more extended and also traces outflowing gas.

We have identified 93 N_2H^+ cores in the field of view, with masses between approximately 0.05 and $2.5 M_\odot$. While uncertainties in the relative abundance of N_2H^+ do not allow us to conclude whether or not individual cores are bound, the trend of core properties suggests that most will be bound. Furthermore, there is no upturn of the distribution of core virial-LTE masses, which would suggest that the lowest mass cores are not bound and therefore transient phenomena. Our conclusion is that even these low-mass cores are likely to remain bound and eventually form stars, or brown dwarfs. If the N_2H^+ cores are bound regardless of mass, this suggests that such emission does not trace transient structures formed out of turbulent fluctuations. Therefore, this implies the entire mass distribution consists of objects that can potentially form stars.

The mass function of the N_2H^+ cores is consistent with the field star IMF, suggesting that the distribution of masses may be locked in at the prestellar phase, in contradiction to theories of mass accumulation by competitive accretion. We find that the mass function of core associated with stars is flat, and unlike the IMF. This may be because lower mass cores lose more of their mass when forming a star, however, further research is required to fully understand this.

We find the relative motions of cores within NGC 1333 to have an rms dispersion of 0.46 km s^{-1} , larger than that found for Oph A by Di Francesco et al. (2004), but the line widths of the cores (average is 0.38 km s^{-1}) are similar to those found in Oph A. We may be seeing an intrinsic increase in relative motions of cores in NGC 1333 but cannot discount the possibility that the larger motions are an artifact of the large size scale probed in NGC 1333.

We have compared the line center velocities of the low-density gas tracers ^{13}CO and C^{18}O to those of N_2H^+ in an attempt to look for relative motions of the high-density N_2H^+ cores with respect to their low-density surroundings, as predicted by some theories of clustered star formation. The relative motions have a dispersion of about 0.55 km s^{-1} , which is smaller than expected if the cores were moving ballistically ($\sim 1.1 \text{ km s}^{-1}$) but larger than the expected dispersion if the cores were not moving ($\sim 0.38 \text{ km s}^{-1}$). We note that the dispersion of core relative velocities may be artificially increased due to differences in beam sizes between the telescopes used to make the measurements. Thus, the data are consistent with no ballistic motions of the high-density cores, but this conclusion needs to be tested more rigorously. We suggest further observations of N_2H^+ and a CO transition may be able to answer this question decisively if the same telescope is used for observations of both transitions, and care is taken to minimize any systematic errors.

We acknowledge the thoughtful comments by an anonymous referee, which have greatly improved the quality of this paper. The BIMA array is operated with support from the National Science Foundation (NSF) under grants AST 99-81308 to the University of California, Berkeley, AST 99-81363 to the University of Illinois, and AST 99-81289 to the University of Maryland. The Five College Radio Astronomy Observatory is supported by NSF grant AST 02-28993. This research has made use of NASA's Astrophysics Data System Bibliographic Services.

REFERENCES

- Aspin, C. 2003, *AJ*, 125, 1480
 Aspin, C., Sandell, G., & Russell, A. P. G. 1994, *A&AS*, 106, 165
 Ballesteros-Paredes, J., & Mac Low, M.-M. 2002, *ApJ*, 570, 734
 Bate, M. R., & Bonnell, I. A. 2005, *MNRAS*, 356, 1201
 Belikov, A., Kharchenko, N., Piskunov, A., Schilbach, E., & Scholz, R.-D. 2002, *A&A*, 387, 117
 Benson, P. J., & Myers, P. C. 1989, *ApJS*, 71, 89
 Bergin, E. A., Alves, J., Huard, T., & Lada, C. J. 2002, *ApJ*, 570, L101
 Beuther, H., & Schilke, P. 2004, *Science*, 303, 1167
 Bonnell, I. A., Bate, M. R., Clarke, C. J., & Pringle, J. E. 1997, *MNRAS*, 285, 201
 ———. 2001a, *MNRAS*, 323, 785
 Bonnell, I. A., Clarke, C. J., Bate, M. R., & Pringle, J. E. 2001b, *MNRAS*, 324, 573
 Caselli, P., Benson, P. J., Myers, P. C., & Tafalla, M. 2002, *ApJ*, 572, 238
 Clarke, C. J., Bonnell, I. A., & Hillenbrand, L. A. 2000, in *Protostars and Planets IV*, ed. V. Mannings, A. P. Boss, & S. S. Russell (Tucson: Univ. Arizona Press), 151
 de Zeeuw, P. T., Hoogerwerf, R., & de Bruijne, J. H. J. 1999, *AJ*, 117, 354
 Di Francesco, J., André, P., & Myers, P. C. 2004, *ApJ*, 617, 425
 Di Francesco, J., Myers, P. C., Wilner, D. J., Ohashi, N., & Mardones, D. 2001, *ApJ*, 562, 770
 Elmegreen, B. G., Efremov, Y., Pudritz, R. E., & Zinnecker, H. 2000, in *Protostars and Planets IV*, ed. V. Mannings, A. P. Boss, & S. S. Russell (Tucson: Univ. of Arizona Press), 179
 Herbig, G. H., & Jones, B. F. 1983, *AJ*, 88, 1040
 Ho, P. T. P., & Barrett, A. H. 1980, *ApJ*, 237, 38
 Jijina, J., Myers, P. C., & Adams, F. C. 1999, *ApJS*, 125, 161
 Johnstone, D., Wilson, C. D., Moriarty-Schieven, G., Joncas, G., Smith, G., Gregersen, E., & Fich, M. 2000, *ApJ*, 545, 327
 Jørgensen, J. K., Hogerheijde, M. R., van Dishoeck, E. F., Blake, G. A., & Schöier, F. L. 2004a, *A&A*, 413, 993
 Jørgensen, J. K., Schöier, F. L., & Dishoeck, E. F. 2004b, *A&A*, 416, 603
 Knee, L. B. G., & Sandell, G. 2000, *A&A*, 361, 671
 Kroupa, P. 2002, *Science*, 295, 82
 Lada, C. J., Alves, J., & Lada, E. A. 1996, *AJ*, 111, 1964
 Lay, O. P., Carlstrom, J. E., & Hills, R. E. 1995, *ApJ*, 452, L73
 Lee, C. W., Myers, P. C., & Tafalla, M. 2001, *ApJS*, 136, 703
 Motte, F., André, P., & Neri, R. 1998, *A&A*, 336, 150
 Ridge, N. A., Wilson, T. L., Megeath, S. T., Allen, L. E., & Myers, P. C. 2003, *AJ*, 126, 286
 Rodriguez, L. F., Anglada, G., & Curiel, S. 1997, *ApJ*, 480, L125
 Salpeter, E. 1955, *ApJ*, 121, 161
 Sandell, G., & Knee, L. B. G. 2001, *ApJ*, 546, L49 (SK01)
 Stanke, T., Smith, M. D., Gredel, R., & Khanzadyan, T. 2006, *A&A*, 447, 609
 Tafalla, M., Myers, P. C., Caselli, P., Walmsley, C. M., & Comito, C. 2002, *ApJ*, 569, 815
 Ulich, B. L., & Haas, R. W. 1976, *ApJS*, 30, 247
 Walsh, A. J., Myers, P. C., & Burton, M. G. 2004, *ApJ*, 614, 194
 Williams, J. P., de Geus, E. J., & Blitz, L. 1994, *ApJ*, 428, 693